

# Manufacturing Letters

Manufacturing Letters 00 (2022) 000-000



50th SME North American Manufacturing Research Conference (NAMRC 50, 2022)

# Template-free scalable fabrication of linearly periodic microstructures by controlling ribbing defects phenomenon during forward roll coating

Md Didarul Islam<sup>a\*\*</sup>, Himendra Perera<sup>b</sup>, Sekkappan Chockalingam<sup>a</sup>, Matthew Phillips<sup>a</sup>, Muh-Jang Chen<sup>a</sup>, Yuxuan Liu<sup>a</sup>, Saad Khan<sup>b</sup>, Yong Zhu<sup>a</sup>, Mohammed Zikry<sup>a</sup>, Jong Eun Ryu<sup>a\*</sup>

<sup>a</sup>Department of Mechanical and Aerospace Engineering, NC State University, Raleigh, NC, 27695, USA

#### **Abstract**

Linear periodic microstructures are of significant importance in various applications, including drag-reduction, biofouling, self-cleaning, and superhydrophobicity. However, practical applications of such surfaces require mass manufacturing techniques, which are highly limited. This study demonstrated a simple template-free scalable manufacturing technique to fabricate linearly periodic microstructure by controlling the ribbing defects in forward roll coating. A viscoelastic polymer nanocomposite with tailored properties was synthesized and utilized as the coating material. The ribbing instabilities were controlled with process parameters that resulted in variable periodicity of the linearly aligned microstructures with a spacing of 114 – 700 µm. The microstructure arrangement also had a linear to random transition as the instabilities increased. The manufactured surface has a high Wenzel roughness factor that ranges from 1.6 to 3.6, which results in water contact angles of 128° to 150°. The linear microstructure films can have critical applications in the mass manufacturing of drag reduction surfaces. The high aspect-ratio microstructure films can also have applications in superhydrophobic, self-cleaning, anti-icing, and anti-biofouling surfaces.

© 2022 Society of Manufacturing Engineers (SME). Published by Elsevier Ltd. All rights reserved.

This is an open access article under the CC BY-NC-ND license (http://creativecommons.org/licenses/by-nc-nd/4.0/)

Peer-review under responsibility of the Scientific Committee of the NAMRI/SME.

Keywords: Scalable manufacturing, periodic microstructure, template-free manufacturing, roll-coating, ribbing, superhydrophobic surfaces

# 1. Introduction

Through many examples of their complex structures used to adapt to the environment, biological systems remain a significant source of inspiration to utilize fundamental scientific principles [1–3]. Nature remains far ahead of human-developed technologies, as natural systems have been using micro-nano scale structures to produce unique functionalities for millions of years [4–6]. For example, lotus leaves have a specific surface roughness with modified surface chemistry to enable self-cleaning [4,7]. Sharks also use microstructures to be

one of the best swimmers in the ocean. They have unique skin morphology with periodic microstructures that modify the nearwall vorticity during turbulent flow, reducing skin friction [8–10]. Namib desert beetles harvest water from the fog with superhydrophobic-superhydrophilic microstructures that allow them to survive in harsh dry weather [11–13]. These unique surface topographies with different functionalities have inspired researchers to develop biomimetic micro-nano structures for applications such as self-cleaning surfaces [14–17], drinking water harvesting from fog [18–20], friction reduction in solid-solid interfaces [9,21,22], and hydrodynamic

<sup>&</sup>lt;sup>a</sup>Department of Chemical and Biomolecular Engineering, NC State University, Raleigh, NC, 27695, USA

<sup>\*</sup> Corresponding author. E-mail address: jryu@ncsu.edu \*\* Co-corresponding author. E-mail address: mislam9@ncsu.edu

drag reduction in ships [8,10,23-25]. While various technologies including photolithography, laser cutting, microcoining, 3D printing, and bio-pattern imprinting have been utilized to fabricate these micro-nano structures, there are critical limitations in practical applications as most of these methods are complex, expensive, and time-consuming, making them unsuitable for mass-manufacturing [26–30]. For example, lithography techniques have been implemented to manufacture periodic linear micro-trench surfaces that have demonstrated drag reduction effects in open-water turbulent flows [31]. However, these surfaces were made from silicon wafers using microelectromechanical systems (MEMS) technology, limiting them to the size of the wafer - that are far smaller than a reallife boat or ship. Manufacturing these micro-patterned structures in a low-cost scalable process is essential for practical applications.

Such desirability of periodic microstructures has motivated for a more insightful look into a common roll-coating defect known as ribbing instability. During the roll-coating process, a positive pressure gradient is developed in the downstream meniscus of the coating fluid [32]. The flow becomes unstable when the pressure gradient exceeds a critical value, and a finger-like growth is observed [33,34]. A visual representation of the ribbing formation is shown in Fig. 1. These spatially periodic patterns transverse to the roll-coating direction are known as ribbing instability [35–38]. Conventionally, these patterns are undesirable in coating applications, such as painting, applying adhesives, or preparing functional films for optical and electrical applications. However, careful controlling of these ribbing patterns could assist in replicating periodic microstructures obtained by the traditional methods.

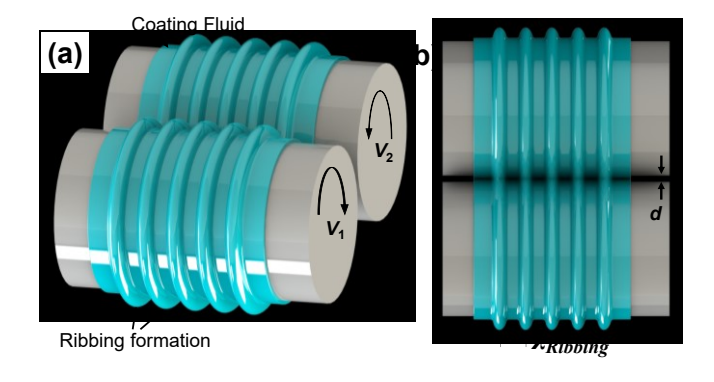


Fig. 1. (a-b) Schematic of the ribbing formation phenomenon on a two-roll coater.

The ribbing behavior of Newtonian and non-Newtonian fluids has been studied through experimental and computational models that aim to minimize roll-coating defects [35–39]. The periodicity, wavelengths, and severity have been studied, which heavily depends on several factors, including the surface energy, viscosity, and shear rate [33,40–42]. Several researchers also identified the capillary number (viscosity × rollers speed / surface tension) as a crucial parameter to describe the on-set condition for the ribbing initiation [34,36,43,44]. A higher capillary number results in a more unstable flow for Newtonian and non-Newtonian fluid.

However, the critical capillary number for non-Newtonian fluid is much lower than Newtonian fluids [44]. The elastic nature of the non-Newtonian coating fluid restricts the flow rate causing a rapid increase in the pressure gradient, which results in more instabilities [32,36,40]. The geometric features such as the roller to roller gap (d) and roller radius (R) is also a critical factor. Often represented in literature as a dimensionless parameter of roller distance to roller radius ratio [36,38,45]. The flow is more susceptible to instabilities at a lower roller gap to radius ratio, as the critical capillary number was found to be lower. This is due to the increase in a pressure gradient that occurs as the fluid flows through a narrower passage, elevating shear stress.

Despite numerous studies, the ribbing formation of non-Newtonian fluids are still not well understood compared to Newtonian fluids [34,38]. Most research on non-Newtonian elastic fluid has focused on identifying the critical capillary numbers or threshold conditions to initiate the instabilities. However, the fluid propagation and ribbing formation beyond the on-set conditions are yet to be explored [46-48]. One primary reason for this limitation is that researchers put efforts into identifying the on-set condition of instabilities to avoid coating defects. Moreover, defining the capillary number and the shear rate appropriately for the roll-coating process is arguable. The shear rate-dependent viscoelastic behavior of the coating materials are usully measured by rheometer. However, the roll-coating instruments are not intrinsically viscometric, as they do not have the necessary sensors. Thus the exact viscosity of the coating paste during the roll-coating process is often unknown. Estimating the capillary number relies on either assuming a constant viscosity or calculating the shear rate based on the velocity gradient of the two rollers [49]. It is inappropriate since it cannot effectively define the shear rate when the two rollers run at the same speed. Accurate measurement of the shear rate can be obtained either by incorporating viscometry to the roll-coater or by finite element analysis to determine the fluid velocity gradient during the rollcoating process [50,51].

The roll-coating method can be used to produce a large surface micro-patterned area by manipulating the ribbinginstability phenomenon. However, there remains a lack of understanding of how the ribbing behavior of non-Newtonian pastes occur. An in-depth investigation of the physical properties of the roll-coating pastes and how it influences the ribbing instabilities in a roll-coating process can achieve scalable manufacturing of periodic micro-patterns surface. Unlike the typical coating applications, this study focuses on going beyond the on-set conditions and carefully controlling the process parameter to manufacture periodic microstructures by controlling the instabilities. One phenomenona observed for Newtonian liquid is that ribbing patterns tend to flatten when the roller stops, as the surface tension dominates over viscosity. However, to manufacture periodic microstructure, it is necessary to retain the deformed shape when the rollers stop. The surface flattening can be avoided by tailoring the coating liquid's viscoelastic properties. Such materials will only behave like a fluid under shear stress but act as solid when the stress is

unloaded. One method to engineer the viscoelasticity of the polymers is nanoparticles addition [52–54]. Previous studies suggest that the volume fraction and geometry of the inclusions influence the rheological properties of the composite. Notably, composites with cylindrical or high aspect ratio nanoparticles are more likely to possess yield properties than spherical particles [55,56].

In this study, the ribbing formation of a Newtonian fluid in a forward roll coating for various process parameters was studied. The finger-like ribbing was observed during the coating. However, when the rollers stopped, the liquid surface flattened due to the surface tension. Thus a viscoelastic composite paste was formulated by adding cylindrical nanoparticles to the Newtonian fluid. This helped to achieve a yield behavior and avoid surface tension-driven flattening. Finally, utilizing the composite paste, linearly periodic microstructures were manufactured by the roll-coating process. An in-depth investigation of the physical properties of the coating paste and roll-coating parameters helped to achieve scalable manufacturing of linearly periodic microstructure surfaces. These surfaces have the great potential to manufacture multifunctional surfaces for reduction. drag superhydrophobicity, self-cleaning, anti-icing coatings, antibiofouling, biological sensors, and radiative cooling.

## 2. Methodology

## 2.1. Coating materials preparation

A nanocomposite paste was synthesized using a polydimethylsiloxane elastomer kit (PDMS Sylgard 184, Dow chemicals) and multi-walled carbon nanotube (CNT, 6-9 nm diameter, and 100-200  $\mu m$  length). The PDMS and CNTs were initially mixed utilizing a universal planetary mixer for 10 minutes. Next, the hardener was introduced as 10:1 ratio with the PDMS, and the combined mixture was mixed further in a high-shear three-roll milling machine. The roller distances were gradually reduced, and the materials were passed through multiple times to ensure adequate dispersion and homogenization of the CNTs. The CNT wt% was varied to get composite pastes with tailored rheological properties.

# 2.2. Forward roll coating

A two-roll coating machine was utilized to fabricate the samples and analyze the ribbing behavior (Fig. 2(a)). The radius (R) of each roller was 25.4 mm. The rollers run with independent motors as the angular speed can be controlled within 0 – 120 rpm. A removable polyimide sleeve was inserted on roller #1 to transfer the composite film after the roll-coating. The coating materials were inserted between two rollers and were introduced to different process conditions by controlling the roller velocities  $V_1$ ,  $V_2$ , and the roller distance of d (Fig. 2(b)). Finally, the composite film with micro-structures was oven cured at 125 °C for 25 minutes (Fig. 2(c)).

## 2.3. Rheology measurement

Steady and dynamic oscillatory rheological experiments were conducted on a TA Instruments Discovery Hybrid-3 rheometer with an 8 mm cross-hatched parallel plate geometry, using a 1000 µm - 2 mm measuring gap. Frequency sweeps were performed from 0.1 – 627 Hz at an oscillatory strain of 1%. According to this oscillatory strain sweep, it was determined to be within the linear viscoelastic regime. The lower limit of frequencies for the low modulus sample(s) was often dictated by the transducer limit of the rheometer. Tests were repeated three times, and standard errors were <5%. Average values are reported. The frequency sweep data was later utilized to get steady shear-rate vs. viscosity data based on the Cox-Merz rule [57].

# 2.4. Surface morphology characterization

The surface roughness and waviness of the samples were characterized by a non-contacting laser scanning confocal microscope (Keyence VK-X1100, 0.5 nm height resolution, and 1 nm width resolution). Several roughness descriptors such as the Wenzel roughness factor (r), the density of peaks (Spd), and arithmetic mean wavelength  $(W\lambda a)$  were evaluated from the laser confocal data. The surface morphology was also investigated with a high-resolution scanning electron microscope (FEI Verios 460 L).

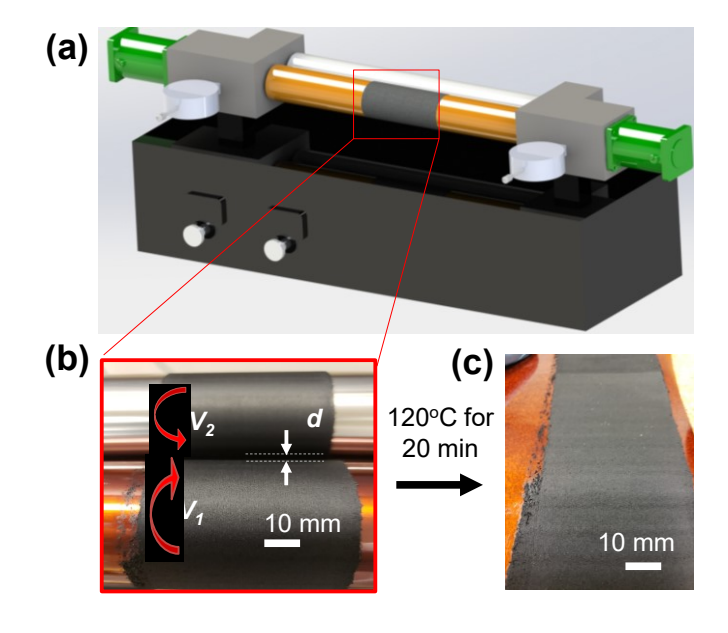


Fig. 2. (a) Two roll coating machines; (b) Forward roll coating of composite paste; (c) Fabricated sample after heat-cure.

#### 2.5. Contact angle measurement

Contact angle measurements were conducted with a Raméhart goniometer (model 250) at ambient temperature (22–25  $^{\circ}$ C). A water droplet of 2  $\mu$ L was carefully deposited onto the sample surface, and the syringe was withdrawn immediately. The water droplet images were taken in 5 different samples' locations by a charge-coupled device camera and a 150 W fiber

optic illuminator. Finally, the water contact angle was measured using the low-bond axisymmetric drop shape analysis plugin provided by the ImageJ software [58].

#### 3. Results

#### 3.1. Rheological properties of PDMS vs. composite paste

The viscoelastic properties of the materials are plotted in Fig. 3. The PDMS showed  $10^{-3}$  to  $10^{-1}$  Pa storage modulus and 1 to  $10^2$  Pa loss modulus from 0.1-100 rad/s angular frequency. As observed, the loss modulus is consistently higher when compared to the storage modulus, which signifies that the PDMS material behaves as a fluid. The viscosity ( $\eta$ ) of the PDMS varies between 5.3-5.2 Pa·s, and change is minimal for the shear rate with a range of 0.1-100 s<sup>-1</sup>.

The 3.5 wt% CNT addition to the PDMS dramatically changes the viscoelastic properties of the materials. The composite shows a storage modulus (G') of  $1.3 \times 10^5 - 6.7 \times 10^5$ Pa and loss modulus (G")  $4.6 \times 10^4 - 9.7 \times 10^4$  Pa. In contrast to the PDMS, the storage modulus is consistently higher than the loss modulus meaning the CNT addition resulted in the materials behaving as a two-phase solid. The viscosity of the 3.5 wt% CNT-PDMS shows a shear-thinning response as viscosity decrease with shear rate. At a low shear, the viscosity is observed to be 106 Pa.s. Whereas, with an increase of shear rate above 600 s<sup>-1</sup>, the viscosity drops to 10<sup>3</sup> Pa.s. The radical reduction in viscosity under shear also indicates a possible yield behavior, meaning above a certain shear-stress the materials to behave as a fluid. The material viscosity is well fitted into power-law as the viscosity was defined by  $2.067 \times 10^{5} (\dot{\gamma}_{0})^{-0.85}$  where  $\dot{\gamma}_{0}$  is the shear rate (s<sup>-1</sup>).

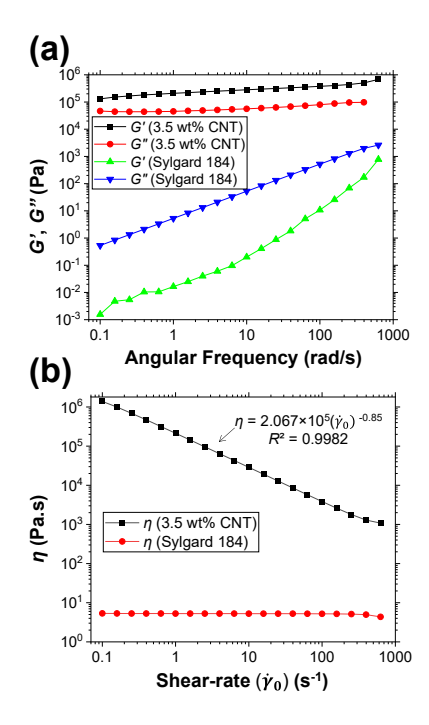


Fig. 3. (a) Storage Modulus (G') and Loss Modulus (G'') vs. angular frequency sweep; (b) Viscosity ( $\eta$ ) vs. the shear-rate data based on Cox-Merz rule

# 3.2. Ribbing instabilities in roll-coating of PDMS

Before diving into the ribbing phenomenon of the complex shear-thinning viscoelastic paste, a full-factorial experiment was conducted to investigate the ribbing of PDMS for various rollers' speeds and roller distance. The rheological properties of PDMS are primarily Newtonian, as the viscosity change during steady shear was minimal. The two roller's speed was kept identical  $(V_1=V_2)$  and varied between 30 and 100 rpm. The roller distance (d) was varied between 0.4-0.8 mm. Upon rotation of the rollers, a distinct ribbing phenomenon was observed. The ribbing wavelengths are defined by the distance between each riblet's peak. Some of the ribbing images are shown in Fig. 4 (a-d). The ribbing wavelength ( $W\lambda_{ribbing}$ ) is investigated in relation to the dimensionless geometric parameter R/d. For any given R/d, an increase in roller speed results in a decrease of  $W\lambda_{ribbing}$  (Fig. (e-f)). A more dramatic reduction in wavelength is observed with the rise of R/d for any specific speed. For example, at R/d 31.75, the wavelength decreases from 7.03 to 6.47 mm with a 30 - 100 rpm roller speed. Whereas, at 30 rpm speed, the wavelength reduces from 7.03 mm to 3.52 mm as the R/d increases from 31.75 to 63.5. This was also noted that at a higher R/d (> 63.5), the ribbing periodicity begins to be nonuniform and random (Fig. 4(d)).

The ribbing pattern of the PDMS is only observed when the rollers are rotating. As soon as the rollers stop, the ribbing patterns flatten in a few seconds due to the surface tension. As observed in section 3.1, the PDMS behaves like a fluid with nearly constant viscosity (5.3-5.2 Pa.s) from a shear rate of 0.1 to 100 s<sup>-1</sup>. This fluid-like behavior allows the surface tension force to flatten the ribbing patterns quickly.

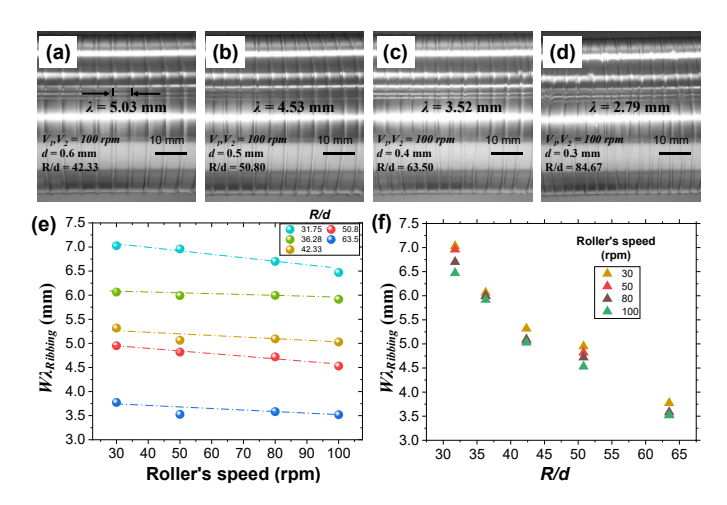


Fig. 4. (a-d) Ribbing instability of PDMS under various process conditions; (e-f) Ribbing wavelengths vs. roller speed. (f) Ribbing wavelengths vs. *R/d* 

In summary, there were two crucial findings from the roll-coating of the PDMS. The wavelength decreases with an increase in roller speed or R/d, whereas the reduction is more evident with the rise of R/d. However, the PDMS can not retain the ribbing patterns when the rollers stop as the materials behave as a fluid. This draws interest in synthesizing coating materials that will behave as a solid when at rest, preventing

surface tension-driven flattening; but acts as fluid during the roll-coating allowing the ribbing formation to occur.

#### 3.3. Ribbing instabilities in roll-coating of composite paste

The CNTs were introduced into the PDMS to tailor the viscoelastic properties of the coating materials. To avoid the surface flattening when the rollers stop, a yielding material is necessary, which will selectively behave like a fluid in elevated shear stress but behave as a solid when the stress is unloaded. The entanglement of the cylindrical-shaped CNTs allowed such behavior. Composite paste with various concentrations of the CNTs was synthesized, and 3.5 wt% of CNT-PDMS were found to be the most suitable one based on viscoelastic properties investigation. The 3.5 wt% CNTs addition on the PDMS ensured the material possessed extremely high viscosity >10<sup>6</sup> Pa.s at low shear-rate, whereas the material's viscosity decreases to 10<sup>3</sup> Pa above 600 s<sup>-1</sup> shear rate. The significantly reduced viscosity under shear allows the materials to behave as fluid during the roll-coating process and facilitates ribbing formation.

A parameter sweep was conducted with different roller speeds (20-100 rpm) and roller distances. At a lower velocity, it was observed that the patterns were more likely to align linearly. Due to a higher capillary number, a higher roller speed induced more instabilities and randomness. In addition, the wavelength control was more precise by controlling the R/d, which is also observed in the roll coating of the PDMS. As a result, the roller's speed was fixed at 20 rpm, while the R/d was varied from 56.44 to 101.6. The roll-coated samples were heat-cured and observed by SEM and laser confocal microscopy to analyze the surface morphology.

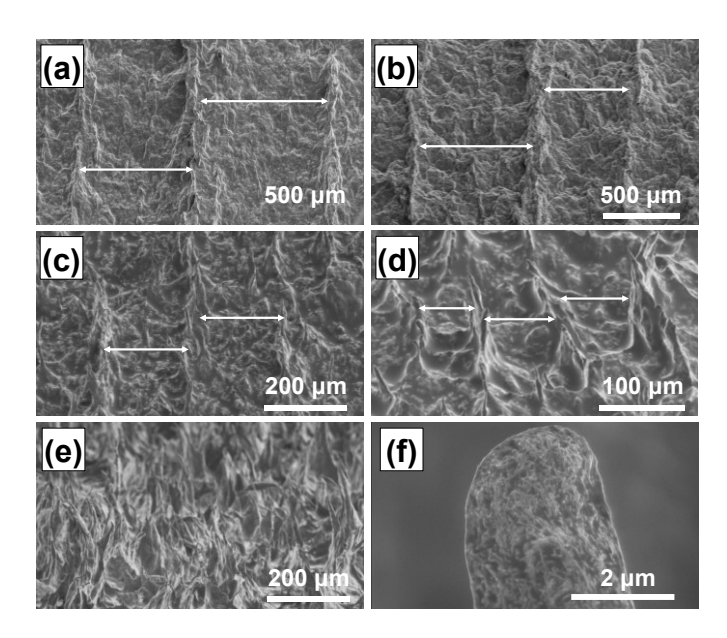


Fig. 5. SEM image of fabricated samples at 20 rpm speed, and (a) R/d = 56.44; (b) R/d = 63.50; (c) R/d = 72.57; (d) R/d = 84.67; (e) R/d = 101.60; (f) entangled CNT dispersion in microstructure peaks.

The 3.5 wt% CNT-PDMS samples showed a hybrid microstructure created by ribbing and capillary bridging. While

the ribbing waves were observed transverse to the roll-coating direction, capillary bridging resulted in many micro-peaks in the longitudinal direction. The SEM images of the samples are shown in Fig. 5. The samples R/d = 56.44, 63.50, 72.57, 84.67 showed mostly linear ribbing formation, whereas the R/d = 101.60 transitions to a more random microstructure. The ribbing wavelengths were reduced from 700  $\mu$ m to 90  $\mu$ m for the linear-microstructure sample (Fig. 5(a-d)). The (R/d=101) sample showed highly dense micro-peaks and a high aspect ratio. The CNTs can be observed at each peak of every sample. Fig. 5(f) shows an example of the micro-peaks observed on the surface. The entangled CNTs allow the PDMS to retain the complex microstructure after roll-coating by resisting the surface tension-driven flattening.

The water contact angles (WCA) of the micro-structured samples were measured to demonstrate the hydrophobicity of the surface (Fig. 6). The measurement was done in 5 different locations for each of the samples. The average WCA was  $128.17^{\circ}$ ,  $133.64^{\circ}$ ,  $136.98^{\circ}$ ,  $137.27^{\circ}$ , and  $150.63^{\circ}$ . The WCA seems to increase with an increase in R/d. However, the trend stalls right before the transition between a linearly periodic microstructure to a high aspect-ratio random microstructure. The WCA dramatically increases into the superhydrophobic range at  $150.63^{\circ}$  for R/d = 101.6.

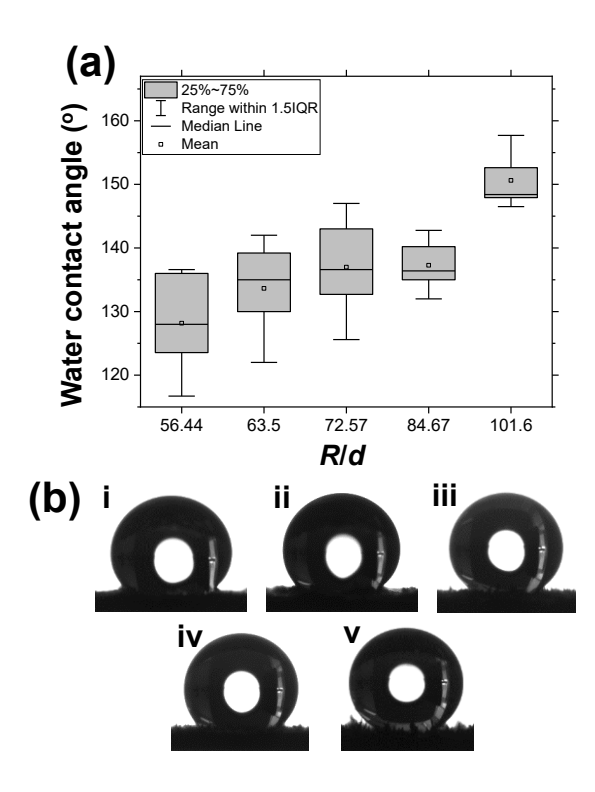


Fig. 6. (a) Water contact angle measurements boxplot in 5 different locations of each sample. (b) Droplet images are the highest contact angle obtained for *R/d* ratio of (i) 56.44, (ii) 63.5, (iii) 72.57, (iv) 84.67, and (v) 101.6.

Since the SEM shows only a small area of the samples, a laser confocal microscope was utilized to quantify the wavelengths and surface roughness. Fig. 7(a) shows an example samples' three-dimensional (3D) topography. The ribbing wavelength ( $W\lambda_{Ribbing}$ ), as described earlier, is defined as the distance between each transverse riblet. The capillary

bridging wavelength ( $W\lambda_{Capillary\ bridging}$ ) is the peak-to-peak distance in the longitudinal direction, as shown in Fig. 7(a). The samples included random microstructures along with the linearly periodic patterns. To quantify the wavelengths, multiple (>20) transverse and longitudinal lines (were drawn on the 3D surface with the Multifileanalyzer software (Keyence). Each of these lines showed the peaks and valleys of the surface topography. The wavelengths for these individual lines are evaluated by the software, and the average values are presented in Fig. 7(c). The wavelengths reduce for both ribbing and capillary bridging phenomenon with an increase in R/d, which is associated with more instabilities. The average  $W\lambda_{Ribbing}$  was 777, 618, 148, 114 µm for the R/d=56.44, 63.50, 72.57, and 84.67 samples. However, when the linear microstructure transitions to a random microstructure at R/d =101.60, the wavelength increases to 224  $\mu m$ . The average  $W\lambda_{Capillary\ bridging}$  also follows the same pattern as the observed wavelengths were 455, 337, 200, 146, and 230 µm for the *R/d*=56.44, 63.50, 72.57, 84.67, and 101.60.

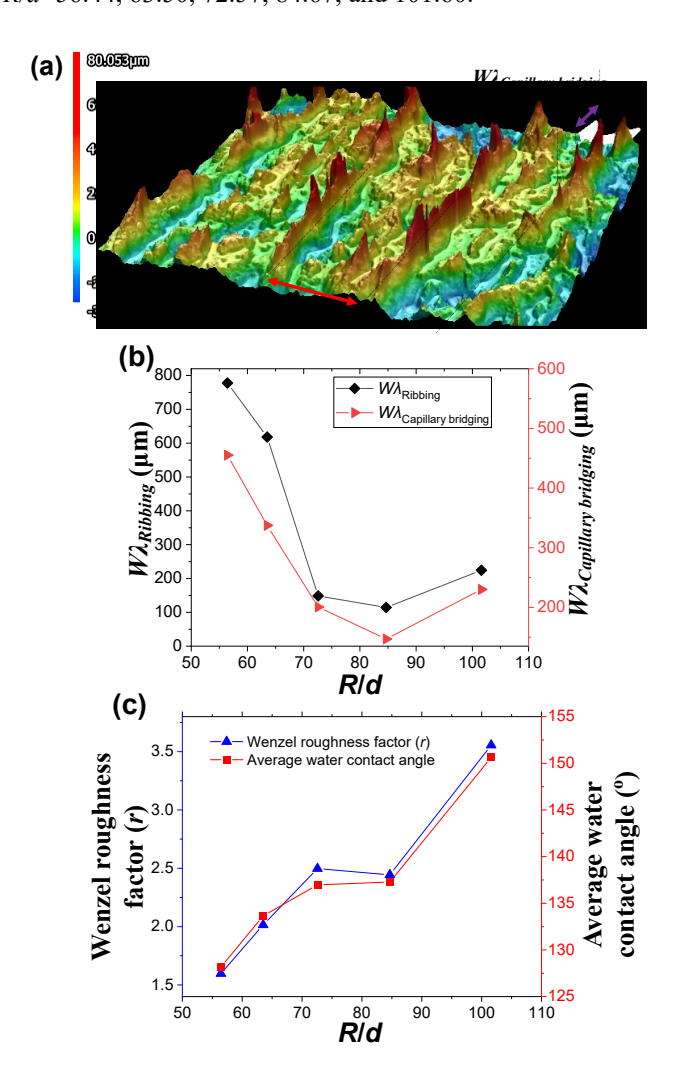


Fig. 7. (a) Laser confocal microscope image of the fabricated sample showing ribbing and capillary bridge formation; (b) Ribbing wavelength, capillary bridging wavelength vs. R/d; (c) Wenzel roughness factor (r), average water contact angle vs. R/d.

The Wenzel roughness factor (r = Actual surface area/cross-sectional area) was also calculated from the 3D

topography of the samples to correlate the hydrophobicity observed from the WCA measurement. The surface roughness increases with increased R/d as the r increases from 1.5 to 3.5 (Fig. 7(c)). However, a dramatic change is observed right after the transition from a linearly periodic microstructure to a random microstructure. This is also reflected in the water contact angle measurement as the (R/d=101.6) sample appears to be superhydrophobic (>150°). The surface roughness and water contact angle measurements closely match each other.

#### 4. Conclusion

Ribbing instabilities were observed initially for the pure PDMS; however, the polymer flattens while resting due to a low viscosity compared to the surface energy. The wavelengths for the PDMS were observed in the 7.03 to 3.52 mm range for roller speeds from 30 to 100 rpm and R/d of 31.75 to 63.50. Increasing the CNT content to 3.5wt% on the PDMS allows the polymer to retain its solid shape even after roll-coating is stopped due to the high viscosity to surface energy ratio. Also, the observed ribbing is at a controllable 114-777  $\mu$ m size. However, as the roller distance decreases even further to increase the R/d to 101.60, the linear ribbing transitions into the random microstructure with a high Wenzel roughness factor of 3.56. The water contact angle of the samples ranged from 128.17° to 150.63°.

This study demonstrated a simple, scalable fabrication process to achieve periodic microstructures. The research helped to carefully identify and narrow down the suitable material composition and process parameters to control the micro-trenches' periodicity. The complete sample preparation takes only half an hour, beginning with the coating paste preparation, roll-coating, and heat-curing. The maximum size achievable with the presented two-roll-coater is 300 mm by 150 mm, only constrained by rollers diameter and length. Taking advantage of the ribbing instabilities, a large periodic microstructured surface can be obtained quickly by employing a more robust roll-coater with continuous substrate-feeding capabilities.

Future work will be focused on fine-tuning the process parameters to improve the control of the surface morphology. The mechanical durability of the fabricated microstructures is also being investigated. Finally, the fabricated samples are also being employed to demonstrate drag-reduction capabilities in miniature model ships, self-cleaning surfaces, and anti-biofouling applications.

# Acknowledgments

This research is based upon work supported by the National Science Foundation under grant no. 2031558. J. Ryu was also supported by the new faculty start-up fund at NC State University and the NCSU Faculty Research and Professional Development award. Part of this work was performed in part at the Analytical Instrumentation Facility (AIF) at North Carolina State University, which is supported by the State of North Carolina and the National Science Foundation (award number

ECCS-2025064). The AIF is a member of the North Carolina Research Triangle Nanotechnology Network (RTNN), a site in the National Nanotechnology Coordinated Infrastructure (NNCI).

#### References

- [1] Y.Y. Yan, N. Gao, W. Barthlott, Mimicking natural superhydrophobic surfaces and grasping the wetting process: A review on recent progress in preparing superhydrophobic surfaces, Adv. Colloid Interface Sci. 169 (2011) 80–105.
- [2] B. Bhushan, Biomimetics: Lessons from Nature an overview, Philos. Trans. R. Soc. A Math. Phys. Eng. Sci. 367 (2009) 1445– 1486.
- [3] C. Zhang, D.A. Mcadams, J.C. Grunlan, Nano/Micro-Manufacturing of Bioinspired Materials: a Review of Methods to Mimic Natural Structures, Adv. Mater. 28 (2016) 8566–8566.
- [4] T. Sun, L. Feng, X. Gao, L. Jiang, Bioinspired surfaces with special wettability, Acc. Chem. Res. 38 (2005) 644–652.
- [5] P. Vukusic, J.R. Sambles, Photonic structures in biology, Nature. 424 (2003) 852–855.
- [6] M. Srinivasarao, Nano-Optics in the Biological World: Beetles, Butterflies, Birds, and Moths, Chem. Rev. 99 (1999) 1935–1961.
- [7] W. Yu, J. Koc, J.A. Finlay, J.L. Clarke, A.S. Clare, A. Rosenhahn, Layer-by-layer constructed hyaluronic acid/chitosan multilayers as antifouling and fouling-release coatings, Biointerphases. 14 (2019) 051002.
- [8] M.D. Ibrahim, S.N.A. Amran, Y.S. Yunos, M.R.A. Rahman, M.Z. Mohtar, L.K. Wong, A. Zulkharnain, The study of drag reduction on ships inspired by simplified shark skin imitation, Appl. Bionics Biomech. 2018 (2018) 1–11.
- [9] X. Li, J. Deng, Y. Lu, L. Zhang, J. Sun, F. Wu, Tribological behavior of ZrO2/WS2 coating surfaces with biomimetic shark-skin structure, Ceram. Int. 45 (2019) 21759–21767.
- [10] G. Liu, Z. Yuan, Z. Qiu, S. Feng, Y. Xie, D. Leng, X. Tian, A brief review of bio-inspired surface technology and application toward underwater drag reduction, Ocean Eng. 199 (2020) 106962.
- [11] K.C. Park, P. Kim, A. Grinthal, N. He, D. Fox, J.C. Weaver, J. Aizenberg, Condensation on slippery asymmetric bumps, Nature. 531 (2016) 78–82.
- [12] D. Gurera, B. Bhushan, Passive water harvesting by desert plants and animals: Lessons from nature, Philos. Trans. R. Soc. A Math. Phys. Eng. Sci. 378 (2020).
- [13] J. Guadarrama-Cetina, A. Mongruel, M.-G. Medici, E. Baquero, A.R. Parker, I. Milimouk-Melnytchuk, W. González-Viñas, D. Beysens, Dew condensation on desert beetle skin, Eur. Phys. J. E. 37 (2014) 1–6.
- [14] T. Wang, L. Huang, Y. Liu, X. Li, C. Liu, S. Handschuh-Wang, Y. Xu, Y. Zhao, Y. Tang, Robust Biomimetic Hierarchical Diamond Architecture with a Self-Cleaning, Antibacterial, and Antibiofouling Surface, ACS Appl. Mater. Interfaces. 12 (2020) 24432–24441.
- [15] Q. Xu, W. Zhang, C. Dong, T.S. Sreeprasad, Z. Xia, Biomimetic self-cleaning surfaces: Synthesis, mechanism and applications, J. R. Soc. Interface. 13 (2016).
- [16] B. Bhushan, Y.C. Jung, Natural and biomimetic artificial surfaces for superhydrophobicity, self-cleaning, low adhesion, and drag reduction, Prog. Mater. Sci. 56 (2011) 1–108.
- [17] B. Bhushan, K. Koch, Y.C. Jung, Biomimetic hierarchical structure

- for self-cleaning, Appl. Phys. Lett. 93 (2008) 093101.
- [18] M.A.K. Azad, D. Ellerbrok, W. Barthlott, K. Koch, Fog collecting biomimetic surfaces: Influence of microstructure and wettability, Bioinspiration and Biomimetics. 10 (2015) 016004.
- [19] L. Zhong, L. Zhu, J. Li, W. Pei, H. Chen, S. Wang, A. Razaa, A. Khan, Y. Hou, Y. Zheng, Recent advances in biomimetic fog harvesting: focusing on higher efficiency and large-scale fabrication, Mol. Syst. Des. Eng. (2021).
- [20] J. Feng, L. Zhong, Z. Guo, Sprayed hieratical biomimetic superhydrophilic-superhydrophobic surface for efficient fog harvesting, Chem. Eng. J. 388 (2020) 124283.
- [21] Y. Lu, Superior lubrication properties of biomimetic surfaces with hierarchical structure, Tribol. Int. 119 (2018) 131–142.
- [22] Z. Guo, C. Yuan, A. Liu, S. Jiang, Study on tribological properties of novel biomimetic material for water-lubricated stern tube bearing, Wear. 376–377 (2017) 911–919.
- [23] M. Xu, B. Arihara, H. Tong, N. Yu, Y. Ujiie, C.J. Kim, A low-profile wall shear comparator to mount and test surface samples, Exp. Fluids. 61 (2020) 1–13.
- [24] C. Lee, C.H. Choi, C.J. Kim, Superhydrophobic drag reduction in laminar flows: a critical review, Exp. Fluids. 57 (2016) 1–20.
- [25] M. Ahmadzadehtalatapeh, M. Mousavi, A Review on the Drag Reduction Methods of the Ship Hulls for Improving the Hydrodynamic Performance, Int. J. Marit. Technol. 4 (2015) 51–64.
- [26] H.S. Hwang, N.H. Kim, S.G. Lee, D.Y. Lee, K. Cho, I. Park, Facile fabrication of transparent superhydrophobic surfaces by spray deposition, ACS Appl. Mater. Interfaces. 3 (2011) 2179–2183.
- [27] S. Kato, A. Sato, Micro/nanotextured polymer coatings fabricated by UV curing-induced phase separation: Creation of superhydrophobic surfaces, J. Mater. Chem. 22 (2012) 8613–8621.
- [28] J. Zou, H. Chen, A. Chunder, Y. Yu, Q. Huo, L. Zhai, Preparation of a superhydrophobic and conductive nanocomposite coating from a carbon-nanotube-conjugated block copolymer dispersion, Adv. Mater. 20 (2008) 3337–3341.
- [29] S. Lee, J. Lee, J. Park, Y. Choi, K. Yong, Resistive switching WOx-Au core-shell nanowires with unexpected nonwetting stability even when submerged under water, Adv. Mater. 24 (2012) 2418–2423.
- [30] L. Zhu, Y. Xiu, J. Xu, P.A. Tamirisa, D.W. Hess, C.P. Wong, Superhydrophobicity on two-tier rough surfaces fabricated by controlled growth of aligned carbon nanotube arrays coated with fluorocarbon, Langmuir. 21 (2005) 11208–11212.
- [31] M. Xu, A. Grabowski, N. Yu, G. Kerezyte, J.W. Lee, B.R. Pfeifer, C.-J.J. Kim, Superhydrophobic Drag Reduction for Turbulent Flows in Open Water, Phys. Rev. Appl. 13 (2020) 034056.
- [32] G.A. Zevallos, M.S. Carvalho, M. Pasquali, Forward roll coating flows of viscoelastic liquids, J. Nonnewton. Fluid Mech. 130 (2005) 96–109.
- [33] R.J. Fields, M.F. Ashby, Finger-like crack growth in solids and liquids, Philos. Mag. 33 (1976) 33–48.
- [34] A.M. Grillet, A.G. Lee, E.S.G. Shaqfeh, Observations of ribbing instabilities in elastic fluid flows with gravity stabilization, J. Fluid Mech. 399 (1999) 49–83.
- [35] M.E. Gurfinkel Castillo, A.T. Patera, Three-dimensional ribbing instability in symmetric forward-roll film-coating processes, J. Fluid Mech. 335 (1997) 323–359.
- [36] Y.H. Chong, P.H. Gaskell, N. Kapur, Coating with deformable rolls: An experimental investigation of the ribbing instability, Chem. Eng. Sci. 62 (2007) 4138–4145.

- [37] T. Bauman, T. Sullivan, S. Middleman, Ribbing instability in coating flows: Effect of polymer additives, Chem. Eng. Commun. 14 (1982) 35–46.
- [38] J. Greener, T. Sullivan, B. Turner, S. Middleman, Ribbing instability of a two-roll coater: Newtonian fluids, Chem. Eng. Commun. 5 (1980) 73–83.
- [39] M. Yamamura, Ribbing instability of Newtonian fluid coated on a topographic surface, J. Coatings Technol. Res. 17 (2020) 1447– 1453.
- [40] J.H. Lee, S.K. Han, J.S. Lee, H.W. Jung, J.C. Hyun, Ribbing instability in rigid and deformable forward roll coating flows, Korea Aust. Rheol. J. 22 (2010) 75–80.
- [41] A.M. Grillet, A.G. Lee, E.S.G. Shaqfeh, Observations of ribbing instabilities in elastic fluid flows with gravity stabilization, J. Fluid Mech. 399 (1999) 49–83.
- [42] M. Rosen, M. Vazquez, Secondary waves in ribbing instability, in: AIP Conf. Proc., American Institute of PhysicsAIP, 2007: pp. 14– 19.
- [43] D.J. Coyle, C.W. Macosko, L.E. Scriven, Reverse roll coating of non-Newtonian liquids, J. Rheol. (N. Y. N. Y). 34 (1998) 615.
- [44] F. Varela López, L. Pauchard, M. Rosen, M. Rabaud, Non-Newtonian effects on ribbing instability threshold, J. Nonnewton. Fluid Mech. 103 (2002) 123–139.
- [45] M.E. Gurfinkel Castillo, A.T. Patera, Three-dimensional ribbing instability in symmetric forward-roll film-coating processes, J. Fluid Mech. 335 (1997) 323–359.
- [46] T. Bauman, T. Sullivan, S. Middleman, RIBBING INSTABILITY
  IN COATING FLOWS: EFFECT OF POLYMER ADDITIVES,
  Http://Dx.Doi.Org/10.1080/00986448208911036. 14 (2007) 35–46.
- [47] D.A. Soules, R.H. Fernando, J.E. Glass, Dynamic Uniaxial Extensional Viscosity (DUEV) Effects in Roll Application I. Rib and Web Growth in Commercial Coatings, J. Rheol. (N. Y. N. Y). 32 (2000) 181.
- [48] D.J. Coyle, Knife and Roll Coating, Liq. Film Coat. (1997) 539–

- 571.
- [49] S.-H. Park, S. Lee, D. Moreira, P.R. Bandaru, I. Han, D.-J. Yun, Bioinspired superhydrophobic surfaces, fabricated through simple and scalable roll-to-roll processing, Sci. Rep. 5 (2015) 15430.
- [50] D.J. Coyle, C.W. Macosko, L.E. Scriven, Film-splitting flows in forward roll coating, J. Fluid Mech. 171 (1986) 183–207.
- [51] D.J. Coyle, C.W. Macosko, L.E. Scriven, Film-splitting flows of shear-thinning liquids in forward roll coating, AIChE J. 33 (1987) 741–746.
- [52] A. Shahsavar, M. Bahiraei, Experimental investigation and modeling of thermal conductivity and viscosity for non-Newtonian hybrid nanofluid containing coated CNT/Fe3O4 nanoparticles, Powder Technol. 318 (2017) 441–450.
- [53] S. Abbasi, S.M. Zebarjad, S.H.N. Baghban, A. Youssefi, M.S. Ekrami-Kakhki, Experimental investigation of the rheological behavior and viscosity of decorated multi-walled carbon nanotubes with TiO2 nanoparticles/water nanofluids, J. Therm. Anal. Calorim. 123 (2016) 81–89.
- [54] B. Jo, D. Banerjee, Viscosity measurements of multi-walled carbon nanotubes-based high temperature nanofluids, Mater. Lett. 122 (2014) 212–215.
- [55] S. Mueller, E.W. Llewellin, H.M. Mader, The rheology of suspensions of solid particles, Proc. R. Soc. A. 466 (2010) 291– 300.
- [56] E. Anczurowski, S.G. Mason, Particle Motions in Sheared Suspensions. XXIV. Rotation of Rigid Spheroids and Cylinders, Trans. Soc. Rheol. 12 (2000) 209.
- [57] W.M. Kulicke, R.S. Porter, Relation between steady shear flow and dynamic rheology, Rheol. Acta 1980 195. 19 (1980) 601–605.
- [58] A.F. Stalder, G. Kulik, D. Sage, L. Barbieri, P. Hoffmann, A snake-based approach to accurate determination of both contact points and contact angles, Colloids Surfaces A Physicochem. Eng. Asp. 286 (2006) 92–103.